Appl. Phys. B 84, 183–189 (2006)
DOI: 10.1007/s00340-006-2191-4

Applied Physics B
Lasers and Optics

C. ROPERS[1]
G. STIBENZ[1]
G. STEINMEYER[1]
R. MÜLLER[1]
D.J. PARK[2]
K.G. LEE[2]
J.E. KIHM[2]
J. KIM[3]
Q.H. PARK[4]
D.S. KIM[2]
C. LIENAU[1,✉]

Ultrafast dynamics of surface plasmon polaritons in plasmonic metamaterials

[1] Max-Born-Institut für Nichtlineare Optik und Kurzzeitspektroskopie, Max-Born-Straße 2A, 12489 Berlin, Germany
[2] School of Physics, Seoul National University, Seoul 151-742, Korea
[3] Korea Research Institute of Standards and Science, Yusung, Taejon 305-600, Korea
[4] Department of Physics, Korea University, Seoul 136-701, Korea

Received: 10 January 2006/Revised version: 3 March 2006
Published online: 25 April 2006 •

ABSTRACT Using near-field scanning optical microscopy and ultrafast laser spectroscopy, we study the linear optical properties of subwavelength nanoslit and nanohole arrays in metal films, which are prototype structures for novel plasmonic metamaterials. Near-field microscopy provides direct evidence for surface plasmon polariton (SPP) excitation and allows for spatial imaging of the corresponding SPP modes. By employing spectral interferometry with ultrashort 11-fs light pulses, we directly reconstruct the temporal structure of the electric field of these pulses as they are transmitted through the metallic nanostructures. The analysis of these data allows for a quantitative extraction of the plasmonic band structure and the radiative damping of the corresponding SPP modes. Clear evidence for plasmonic band gap formation is given. Our results reveal that the coherent coupling between different SPP modes can result in a pronounced suppression of radiative SPP damping, increasing the SPP lifetime from 30 fs to more than 200 fs. These findings are relevant for optimizing and manipulating the optical properties of novel nano-plasmonic devices.

PACS 42.70.Qs; 07.79.Fc; 42.25.-p

1 Introduction

Surface-bound electromagnetic waves on metals, so-called surface plasmon polaritons (SPPs), are the elementary optical excitations of novel plasmonic nanostructures. Such plasmonic structures promise an unprecedented amount of microscopic light control [1–4] and applications in, e.g., nano-lensing [3], perfect lensing [5], field localization, and ultrafast switching. Nano-hole and -slit arrays in metal films are particularly important model systems for SPP nano-optics, and the enhanced transmissiom of light [4] through such arrays is one of the many unusual optical phenomena associated with this class of nanostructures. Recent time-resolved experiments have demonstrated a strong SPP coupling to far-field radiation [6], limiting SPP lifetimes to few tens of femtoseconds [6–8]. This poses a serious constraint on using these structures in novel elements such as plasmonic resonators or nano-waveguides. The question arises of how to control radiative SPP damping in order to overcome these lifetime constraints.

In this paper, we give a full account of recent experiments [6, 9, 10] addressing this question by spatially and temporally analyzing light transmission through plasmonic crystals. Specifically, we report on an amplitude- and phase-resolved study of the electric field of ultrashort 11-fs light pulses transmitted through metallic nanoslit and -hole arrays [10]. These experiments give evidence for two interfering transmission channels: ultrafast non-resonant transmission due to photon tunneling and time-delayed resonant reemission from SPP excitatons. The analysis of these measurements allows to reconstruct the plasmonic bandstructure of these crystals and evidences band gap formation. We demonstrate that – in addition to band gap formation – the coherent coupling between different SPP modes induced by periodic variations in the dielectric function can also result in a pronounced enhancement of the radiative SPP lifetime, increasing from 30 to more than 200 fs. Near-field optical images reveal that the formation of coupled, antisymmetric SPP modes is the origin of this radiative damping suppression, in analogy to Dicke subradiance [11] in coupled atomic and molecular systems.

The article is structured as follows: In Sect. 2 we describe our experimental techniques. In Sect. 3 we demonstrate the use of near-field scanning optical microscopy for direct imaging of SPP eigenmodes in plasmonic crystals. Section 4 reports and discusses results on ultrafast light transmission through periodic nanoslit arrays. Some conclusions are given in Sect. 5.

2 Experimental

We investigate 150 nm thick gold films that are either perforated by periodic square arrays of nanoholes with a radius of 125 nm and periods of 700 to 800 nm or by linear arrays of 50-nm wide nano-slits and 600 to 900 nm periods Fig. 1. The samples are fabricated by dry etching after e-beam patterning of a gold film grown on a $\lambda/5$ flat sapphire substrate [6, 9]. The linear optical properties of these nanostructures are studied by both, conventional far-field white-light spectroscopy and near-field scanning optical microscopy (NSOM). In the NSOM measurements, the sample is illuminated with linearly polarized light from a spectrally tunable continuous-wave Ti:sapphire laser through the sapphire

✉ Fax: +49-30-6392-1489, E-mail: lienau@mbi-berlin.de

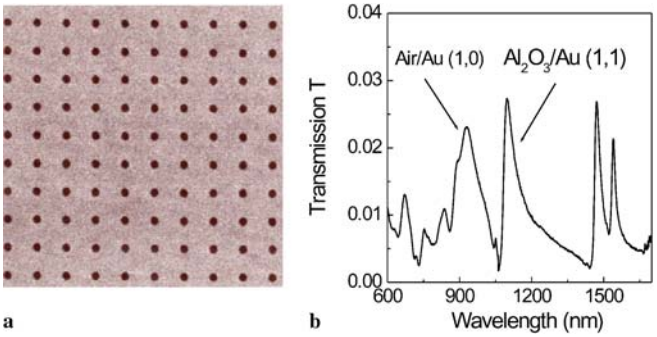

FIGURE 1 (**a**) Scanning electron microscope image of a periodic nanohole array in an optically thick gold film. The array period is 850 nm and the hole diameter 150 nm. (**b**) Representative far-field transmission spectrum through such an array in a 300-nm thick gold film deposited on a sapphire substrate. The spectrum is recorded near normal incidence and transmission resonances at either the air/gold or sapphire/gold interface are indicated

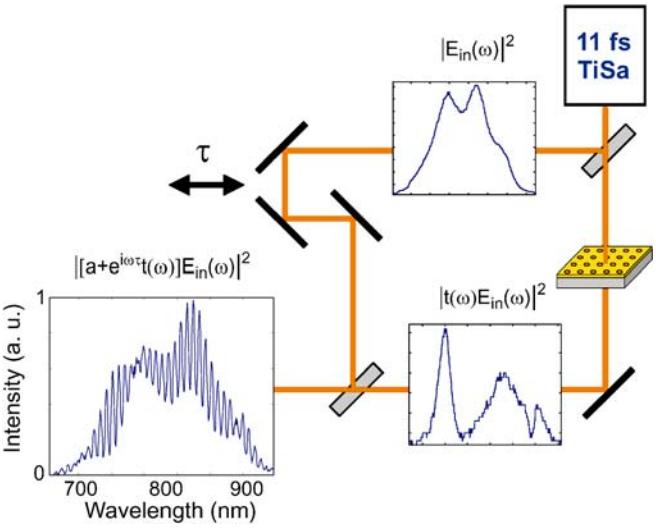

FIGURE 2 (**a**) Schematic of the experimental arrangement for measuring the time structure of the electric field transmitted through a periodic nanoslit/-hole array. In one arm of a Mach–Zehnder interferometer, the incident 11-fs pulses of a Ti:sapphire oscillator are weakly focussed onto the investigated sample using reflective metal optics. The spectral interferogram of the transmitted pulses and the time-delayed replica of the incident pulses is analyzed in a spectrograph connected to a fast line-scan camera. Representative spectra of the 120-nm bandwidth incident pulses and of the transmitted pulses are shown in the insets, together with a typical spectral interferogram

substrate. The incident beam is focused to a spot size of about 10 μm, and the electric field at the metal/air interface is coupled into an aluminum-coated near-field probe with an 80–100 nm aperture diameter. The signal is then detected with a silicon avalanche photodiode. A conventional tuning-fork-based shear-force distance regulation is used to maintain a constant tip-to-sample distance of about 10 nm. All experiments are performed at room temperature.

In the time-resolved experiments, ultrashort 11-fs light pulses from a Ti:sapphire oscillator centered at a wavelength of 800 nm are transmitted through the metallic nanostructures. The linearly polarized pulses are weakly focused onto the sapphire substrate of the sample using reflective metal optics at an angle θ with respect to the grating normal. Both, amplitude and phase of the incident electric field are fully characterized by spectral phase interferometry for direct electric-field reconstruction (SPIDER) [12, 13], apart from an unknown carrier-envelope phase. The time structure of the transmitted light is investigated as a function of the angle of incidence θ by interferometric autocorrelation (IAC) [14] and spectral interferometry (SI) [15, 16]. In SI, an interferogram of the transmitted pulses and the time-delayed replica of the incident pulses is generated in a Mach–Zehnder interferometer (Fig. 2), dispersed in an 0.5 m spectrograph and detected by a fast 2048 pixel line-scan camera, covering the wavelength range from 700 to 900 nm in a single shot. A read-out rate of 1 kHz is sufficient to avoid any degradation of the fringe visibility in the unstabilized interferometer (see inset in Fig. 2). In this way, the amplitude and phase of both, the incident pulse and the transmission function of the nanoslit array are known, and we can compute the electric field at the output of the array and determine its temporal structure via a Fourier transform.

3 Near-field mapping of surface plasmon polariton modes

A typical far-field transmission spectrum of a sample with 150 nm hole diameter and a period of 850 nm perforated into a 300 nm thick gold film, is displayed in Fig. 1b. It shows pronounced transmission resonances at certain resonance wavelengths [4]. Surprisingly, it was found that this transmission is so large that it may even exceed the geometrical filling fraction of the nanoholes in the metal film [4]. The resonant transmission enhancement arises from an efficient grating coupling of the incident far-field radiation to surface-plasmon-polariton (SPP) excitations at either the air-metal or sapphire-metal interfaces. The resonance energies can be estimated [17] from the SPP dispersion relations on a planar metal-dielectric interface $\omega(\boldsymbol{k}_{\mathrm{SP}}) = c|\boldsymbol{k}_{\mathrm{SP}}| \left(\frac{\varepsilon_{\mathrm{m}}+\varepsilon_{\mathrm{d}}}{\varepsilon_{\mathrm{m}}\varepsilon_{\mathrm{d}}}\right)^{1/2}$, energy conservation $\omega(\boldsymbol{k}_{\mathrm{SP}}) = \omega_{\mathrm{L}}$, and momentum conservation $\boldsymbol{k}_{\mathrm{SP}} = \boldsymbol{k}_{\parallel} \pm p\boldsymbol{G}_{\mathrm{x}} \pm q\boldsymbol{G}_{\mathrm{y}}$. Here ω_{L} denotes the frequency of the incident light with in-plane wave vector $\boldsymbol{k}_{\parallel}$. $\omega(\boldsymbol{k}_{\mathrm{SP}})$ is the frequency of the SPP with wave vector $\boldsymbol{k}_{\mathrm{SP}}$, and ε_{m} and ε_{d} are the dielectric function of metal and dielectric, respectively. $\boldsymbol{G}_{\mathrm{x}}$ and $\boldsymbol{G}_{\mathrm{y}}$ are the reciprocal lattice vectors, i.e., in this case $|\boldsymbol{G}_{\mathrm{x}}| = |\boldsymbol{G}_{\mathrm{y}}| = 2\pi/a_0$, where a_0 is the grating period. The integers p and q indicate the amount of momentum transferred by the grating. Consequently, the different transmission resonances are labelled as AM$[p, q]$ and SM$[p, q]$ for excitation of SPP modes at the air and sapphire side, respectively. For slit structures, only the in-plane wave vector component perpendicular to the slit axis is affected and the resonances are labelled AM$[p]$ and SM$[p]$, correspondingly. The above estimate of the resonance positions is only an approximation as the experimentally observed transmission maxima are affected by (i) the hole-induced change of the planar surface dispersion relation, (ii) hole-induced couplings of different SPP modes (i.e., band gap formation), and (iii) the finite radiative damping of these SPP modes, as will be seen in the next section.

As the role of SPP excitations in this enhanced-transmission process has been the subject of a considerable amount of theoretical work [18–22], partly reaching seemingly controversial conclusions [20, 21], there is some interest in giving direct experimental evidence for SPP excitations in nanohole-

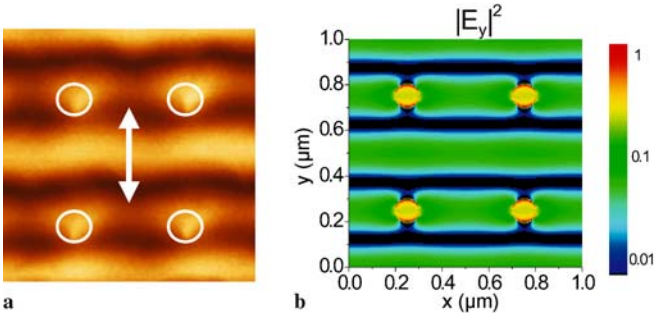

FIGURE 3 (**a**) Image of the transmitted intensity in the near-field of a two-dimensional array of nanoholes of 150 nm diameter with a period of 850 nm in a 300 nm thick gold film. The image is recorded at an excitation wavelength of 877 nm with an aluminum-coated NSOM fiber probe with an ~ 80 nm aperture diameter. The polarization direction of the incident light is indicated. (**b**) Near-field intensity $|E_y|^2$ on top of a hole-perforated metal film from a three-dimensional finite difference time domain simulation. The simulation was performed for a silver grating with a 500 nm period and a 100 nm hole diameter. The incident wave at 530 nm is polarized along the y-direction

perforated metal films. This can be achieved by imaging the electric field intensity in the near-field of the metal film [9]. Figure 3a shows such a near-field image taken on an array of nanoholes with 150 nanometer diameter and a grating period of $a_0 = 850$ nm. In this experiment, the laser light is sent at near-normal incidence through the sapphire substrate, and the transmitted light is collected with an aluminum-coated tapered fiber probe with ~ 80 nm aperture diameter. The excitation wavelength is 877 nm, close to the AM[1, 0] resonance. The linear laser polarization (along the x-direction) and the location of the nanoholes, precisely known from simultaneously recorded shear-force images, are indicated in the figure. This quite striking result gives indeed clear evidence for efficient SPP excitation. Only a small fraction of the total light intensity is detected inside or near the nanoholes, whereas most of the light intensity is found on the metal surface, away from the holes. The SPP field at the metal surface reveals a clear standing-wave pattern, easily recognized as essentially being dominated by interference of SPP modes with in-plane wave vectors $\boldsymbol{k}_{\mathrm{SP}} = \pm \boldsymbol{G}_{\mathrm{y}}$. The analysis of the dependence of these near-field images on the incident laser polarization (Figure 2 in [9]) supports this assignment. Rotation of the incident polarization by 90° essentially rotates the SPP standing wave pattern. The stripe-like interference pattern is again perpendicularly oriented to the incident polarization, directly evidencing the longitudinal character of surface plasmon polariton waves at metal-/dielectric interfaces [23]. More complicated interference patterns at intermediate polarization angles essentially result from the interference of SPP waves with $\boldsymbol{k}_{\mathrm{SP}} = \pm \boldsymbol{G}_{\mathrm{x}} \pm \boldsymbol{G}_{\mathrm{y}}$.

Since these near-field images are quite different from previous near-field studies with non-resonant excitation in chromium films [24] and also from recent theoretical calculations of the near-field distribution [19], we decided to perform three-dimensional finite difference time domain (FDTD) [25] simulations of light transmission through subwavelength hole arrays [26, 27]. Results for light transmission through 100-nm holes in a free-standing silver film of 100 nm thickness are shown in Fig. 3b. The field distributions for a linear incident polarization along the y-axis, as in Fig. 3a, are calculated by numerically integrating Maxwell's equations in the time domain assuming a Drude model for the dielectric function of the metal. These simulations show that the field distribution close to the aperture is rather well described by the classical Bethe–Bouwkamp model [28, 29] and shows the typical divergence at the rim of the aperture. In addition, strong SPP fields are generated on the non-illuminated side and the stripe-like patterns run perpendicular to the polarization direction. The formation of a standing-wave SPP field is clearly visible in the local enhancement of the field intensity along lines in the center between adjacent holes, perpendicular to the incident y-polarization, in quite good agreement with the experimental results. There are two minor deviations from the theoretically predicted scenario which are readily explained. Experimentally, we do not observe the predicted field divergence at the rims of the aperture. The simulated field intensities in this region are also higher than the measured ones. Clearly, the finite spatial resolution of the used near-field probes may effectively smear out the divergences and, thus, reduce the intensity near the rim of the aperture features. Also, the shape of the experimentally fabricated cylindrical apertures is certainly less ideal than that in the model calculations, and this is likely to suppress the predicted field divergencies even more. It is interesting to note that the experimental results agree quite well with the numerical simulations of the in-plane components of the electric field. This indicates that the used aperture-type NSOM probes are not sensitive to the strong out-of-plane "z"-polarized field components, generated in the near-field of the metal film. These field components are expected to display a different spatial distribution [26] and may be probed, e.g., via second-harmonic generation at sharp metal tips [30].

Despite the convincing agreement between experiment and theoretical simulation, one may be sceptical whether the used near-field probes really serve as such an efficient polarization filter for the in-plane field components. In fact, a recent experimental and theoretical study of light transmission through periodic arrays of metal nanoparticles [31] apparently reached a different conclusion. Recently, we have, therefore, analyzed this point in detail by recording spectrally-resolved images of light transmission through periodic nanoslit arrays as a function of distance between tip and metal surface. This study, which will be discussed in detail elsewhere, confirms unambiguously that – in our experimental geometry – in-plane field components are indeed selectively imaged. This study also evidences the absence of tip-induced modifications of the transmission spectra, which may be expected due to tip-SPP couplings. In the next section we make use of this near-field imaging technique for studying the effects of coherent SPP coupling on the optical properties of such arrays.

4 Ultrafast dynamics of light transmission through plasmonic metamaterials: Tuning radiant damping by coherent SPP coupling

To study the ultrafast dynamics of light propagation through such metallic nanostructures, we first probe the time structure of the transmitted light by a second-order interferometric autocorrelation (IAC) technique commonly applied for the characterization of ultrashort laser pulses (Fig. 4). As a model system, we study light propagation

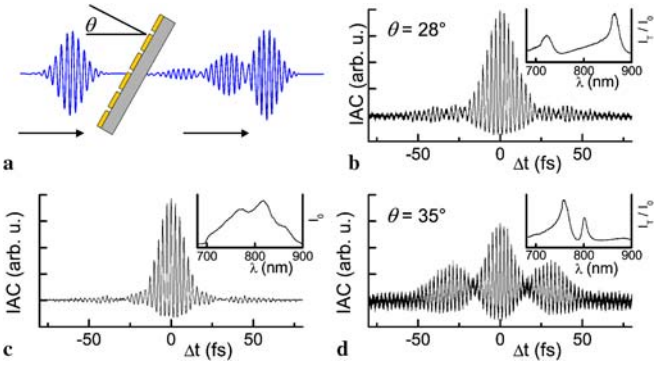

FIGURE 4 (**a**) Schematic of the time-resolved transmission experiments. The time structure of the 11-fs incident pulses and of the pulses transmitted through an array of 50-nm wide slits in a 100-nm thick gold film is characterized by interferometric autocorrelation (IAC). (**b**) IAC and spectrum (*inset*) of the incident laser pulses. (**c**) IAC and spectrum of the transmitted light at $\theta = 28°$. (**d**) IAC and spectrum at $\theta = 35°$. At this angle, the IAC trace is dominated by the re-emission from resonant SPP excitations

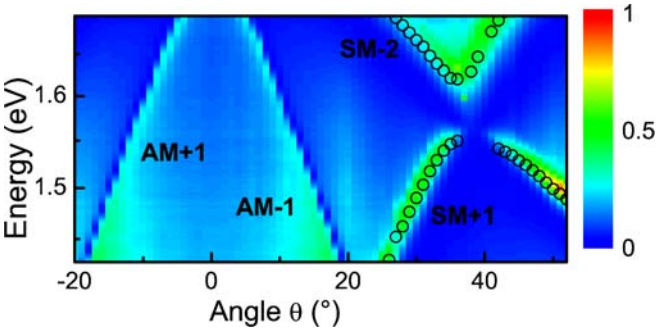

FIGURE 6 Angle-resolved transmission spectrum $T(\omega, \theta)$ for a gold nanoslit array with a period of $a_0 = 650$ nm and a slit width of 50 nm. The sample thickness is 150 nm. *Open circles*: Calculated SPP bandstructure $\omega_j(\theta)$ near the crossing of SM[+1] and SM[−2] resonances. A band gap splitting of $V_g \simeq 72$ meV is revealed. Note the spectral narrowing of the transmission spectrum and the decrease in transmission intensity in the lower energy region of the SM[+1]/SM[−2] crossing

through a linear array of 50-nm wide nanoslits in a 150-nm thick gold film. In these experiments, the transmitted light is split into two pulses of equal intensity in a Michelson interferometer. Theses pulses are then collinearly overlapped and focused onto a nonlinear optical crystal. The intensity of the generated blue second-harmonic light is measured as function of the variable pulse delay Δt between the two interferometer arms [14, 33, 34]. The IAC trace of the incident 11-fs pulses is shown in Fig. 4b together with the spectrum of the laser pulses. Autocorrelation traces of the light transmitted through the nanoslits at two different incident angles are given in Fig. 4c,d. The normalized linear transmission spectra of the arrays are shown in the insets. At an angle of 28°, the laser spectrum overlaps only weakly with the SM[−2] and SM[+1] SPP resonances at 730 nm and 860 nm, respectively (cf. Fig. 6). Here the transmitted light consists of an ultrafast initial burst and a second long-lived but weak contribution. When the overlap between SPP resonances and laser spectrum is optimized by angle tuning [Fig. 5d], the long-lived contribution is strongly enhanced. Clearly, the transmitted light is now dominated by the pronounced polarization interference between the electric fields re-emitted from the two long-lived SPP resonances, persisting for more than 80 fs.

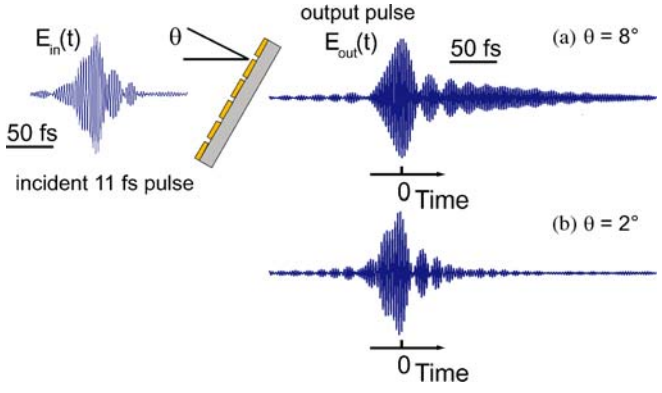

FIGURE 5 (*left*) Measured time structure of the electric field $E_{in}(t)$ of the incident 11-fs pulses with a center wavelength of 800 nm. The amplitude and the phase of $E_{in}(t)$ are characterized by SPIDER. (*right*) Time structure of the pulses $E_{out}(t)$ transmitted through a nanoslit array with $a_0 = 650$ nm for two different angles of (**a**) θ of 8° and (**b**) θ of 2°. The time structure is reconstructed from the spectral interferogram between transmitted and incident pulses (see Fig. 2). The intial burst ("direct transmission") and the delayed reemission from different, interfering SPP resonances are distinguished

These experiments present the first direct visualization of the ultrafast dynamics of light propagation through such metallic nanostructures. Yet, a quantitative reconstruction of the time structure of the transmitted fields is virtually impossible, even if independent knowledge of the power spectrum is available, because different pulse shapes with equal spectrum may yield basically indistinguishable interferometric autocorrelation traces [35]. We, therefore, used spectral interferometry ([15, 16]) with an amplitude- and phase-characterized ultrafast reference pulse for a quantitative retrieval of the transmitted electric field [10] (Fig. 2). The time structures of the incident laser field and the transmitted electric field through a slit array with $a_0 = 650$ nm are shown in Fig. 5 for two different angles of incidence θ. Again, the temporal profile of the transmitted field reveals two distinct components: an initial ultrafast burst mainly around time zero and a long-lived signal persisting beyond 30 fs, which is due to resonant SPP re-emission. Two distinct pathways can contribute to the transmission through these arrays [37, 38]: an ultrafast, nonresonant direct transmission through the nanoslit waveguide $\boldsymbol{E}_{nr}(t)$ and resonant excitation and subsequent reemission of more weakly damped SPP resonances $\boldsymbol{E}_{SP}(t) = \sum_j \boldsymbol{E}_j \exp(-i\omega_j t - \Gamma_j t)$. The total transmitted field $\boldsymbol{E}_t(t) = \boldsymbol{E}_{nr}(t) + \boldsymbol{E}_{SP}(t)$ then results from the interference between both channels. The results in Figs. 5a and b show that the time structure of the transmitted pulses is sensitive to even very small changes of the incidence angle. Both the amplitude of the non-resonant, direct transmission component (almost completely dominating the transmission at $\theta = 2°$) and that of the resonant SPP reemission, as well as the damping time of the SPP reemission can show strong variations for even small angle changes. Both curves have been recorded in a regime, where the direct transmission is strong. For angles between 25° and 40°, however, the transients mainly reflect the long-lived SPP reemission.

In the spectral domain, this interference between a resonant channel and a spectral continuum gives rise to asymmetric Fano-like lineshapes in the far-field transmission spectra

$T(\omega) = |t(\omega)|^2$ with the transmission coefficient

$$t(\omega) = a_{\mathrm{nr}} + \sum_{\mathrm{j}} \frac{b_{\mathrm{j}} \Gamma_{\mathrm{r,j}} e^{\mathrm{i}\phi_{\mathrm{j}}}}{\omega - \omega_{\mathrm{j}} + i(\gamma_{\mathrm{j}} + \Gamma_{\mathrm{r,j}})} \,. \tag{1}$$

In (1), the first and second term are obtained by Fourier transformation of $\boldsymbol{E}_{\mathrm{nr}}(t)$ and $\boldsymbol{E}_{\mathrm{SP}}(t)$, respectively. The resonance width $\Gamma_{\mathrm{j}} = \gamma_{\mathrm{j}} + \Gamma_{\mathrm{r,j}}$ generally contains two contributions: a nonradiative damping γ_{j} due to absorption in the metal and the radiative damping $\Gamma_{\mathrm{r,j}}$ of the SPP modes, which is in most cases dominant [6]. Such a Fano-model allows one to quantitatively describe the distinct asymmetric line shapes of the transmission spectra (Fig. 1) [10, 38], and this quantitative understanding of the line shape function is the key to analysis of coherent couplings between different SPP modes in plasmonic crystals.

To investigate band gap formation and radiative decay phenomena, we have performed angle-resolved spectral interferometry, measuring both amplitude and phase of the field transmission $t(\omega)$. In such experiments, the in-plane momentum $k_{\mathrm{x}} = \frac{\omega}{c} \sin\theta + p\, 2\pi/a_0$ and thus the resonance energy of the excited SPP mode is continuously varied by changing the angle of incidence θ, allowing for a mapping of the SPP band structure [4, 17]. Figure 6 shows transmission spectra $T(\omega, \theta)$ between 700 and 900 nm. Resonances connected to SPPs on both sides of the gold film, namely AM[$p = \pm 1$] and SM[$p = \pm 1, 2$], are clearly resolved. Interestingly, even fine details in these spectra are reproduced when comparing samples with similar structural parameters. In Fig. 7 we show angle-resolved transmission spectra for a series of four slit samples (50 nm slit width) with grating periods varying between 760 nm (a) and 820 nm (d). Essentially, we only find the expected shift in resonance frequency when changing the grating period. The line shape of the different resonances is basically identical in all four samples.

At all angles, both the spectra $T(\omega, \theta)$ as well as the phase of the transmission function $t(\omega, \theta)$ [reported in [10]] are consistently modeled by (1), taking the relevant SPP resonances into account. This analysis allows for a precise measurement of the SPP band structure $\omega_{\mathrm{j}}(\theta)$. The resulting frequencies near the crossing of SM[+1] and SM[−2] around 36° are plotted as open circles in Fig. 6. One observes a clear anti-crossing of the SPP bands with a band gap energy of about 72 meV. Interestingly, there are pronounced variations of the intensities and linewidths near the crossing of the two modes. In particular, as θ approaches the crossing, the lower energy mode becomes narrower until the transmission intensity begins to decrease. As discussed below, this reduction in linewidth reflects the suppression of radiative SPP damping due to the coupling of the SM[+1] and SM[−2] resonances.

Both band gap formation and subradiant SPP decay are expected to be intimately connected with the formation of new coupled SPP eigenmodes of different spatial symmetry [11, 39]. To demonstrate this link, we have studied the damping suppression in more detail near the crossing of two air-metal bands, where we can directly compare the results of the far-field transmission to near-field images of the SPP modes. In order to overlap the AM[+1]/AM[−1] crossing with our laser spectrum, these data are taken on a sample with $a_0 = 750$ nm, red-shifting all transmission resonances by about 100 nm.

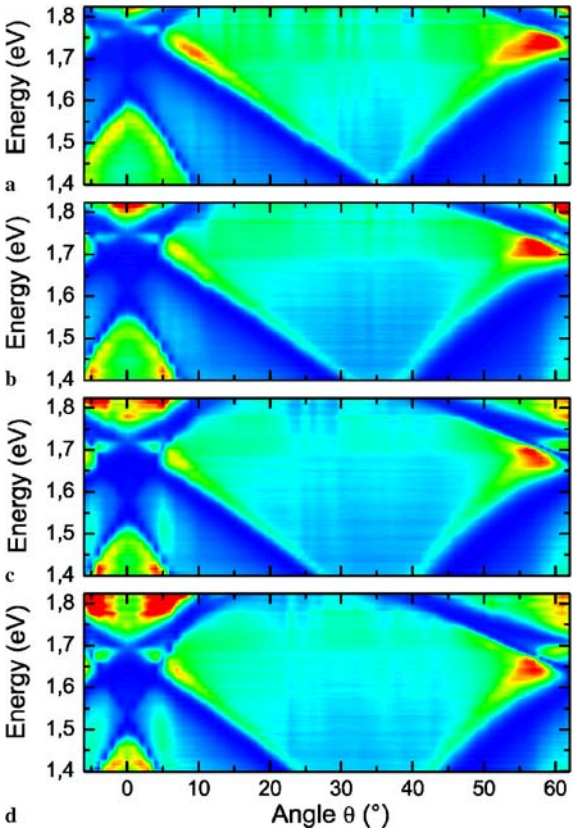

FIGURE 7 Experimentally measured angle-resolved transmission spectrum $T(\omega, \theta)$ for a series of gold nanoslit arrays with a slit width of 50 nm and grating periods of (**a**) $a_0 = 760$ nm, (**b**) 780 nm, (**c**) 800 nm, and (**d**) 820 nm. The sample thickness is 150 nm

Here the far-field transmission spectra near normal incidence (Fig. 8a) show two asymmetric transmission peaks, a spectrally broad and intense low energy resonance at 1.55 eV (bright mode) and a much narrower and weaker high energy peak at 1.62 eV (dark mode). Angle-dependent far-field spectra displayed in Fig. 8b reveal a drastic change in linewidth of the dark mode for small incidence angles. This corresponds to a seven-fold increase in SPP lifetime $T_1 = 1/(2\Gamma)$ to more than 200 fs when θ is reduced from 1.2 to 0.5 degrees (Fig. 8c).

To clarify the microscopic origin of the observed suppression of radiative damping, it is instructive to consider a phenomenological coupled mode model. We first look at the SPP eigenmode solutions of Maxwell's equations for the nanoslit arrays. For vanishing slit width these are simply evanescent plane SPP modes $|j\rangle$ with frequencies ω_j, a nonradiative damping γ_{j} and electric field profiles $\boldsymbol{E}_j(\boldsymbol{r})$ [23]. For simplicity, we consider only two nearly resonant modes $|1\rangle$ and $|2\rangle$, e.g., the AM[± 1] modes in case of Fig. 8. The change in the dielectric function induced by the nanoslits locally changes the electromagnetic energy density and thus leads to frequency shifts V_{11} and V_{22} and, most importantly, to a coupling V_{12} of the two modes. To first order, the strength of these interactions can be approximated as $V_{\mathrm{ij}} \simeq \langle i|\varepsilon^2 \Delta(\varepsilon(\boldsymbol{r})^{-1})|j\rangle/\hbar$ [40], even though some care is needed in using such approximations for metallic nanostructures. Here $\Delta\varepsilon(\boldsymbol{r})$ denotes the local perturbation of the dielectric function.

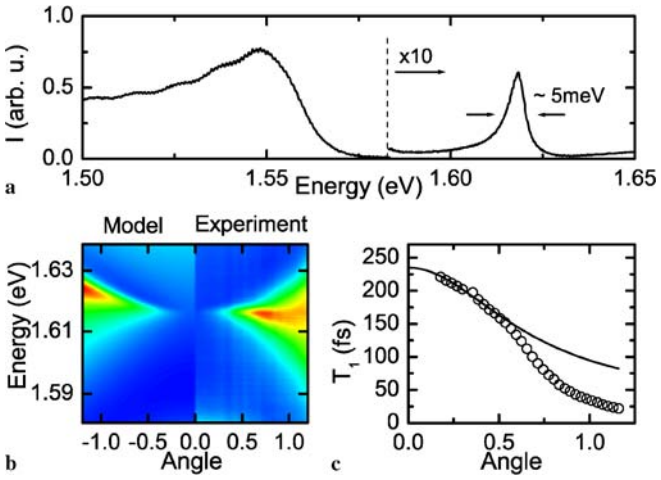

FIGURE 8 (**a**) Transmission spectrum $T(\omega)$ of a gold nanoslit array with $a_0 = 750$ nm, a slit width of 50 nm and 150 nm film thickness near normal incidence ($\theta \sim 0.5°$). (**b**) Experimentally measured angle-dependent transmission spectra in the spectral region of the "dark" transmission resonance (*right*) compared to simulations based on the coupled mode model (2). (**c**) Experimentally determined SPP lifetime $T_1(\theta) = 1/[2(\gamma + \Gamma_r)]$. A small variation of the incidence angle θ by about 1° increases the SPP lifetime by almost one order of magnitude

Moreover, the nanoslits induce a coupling of the evanescent SPP modes of the ideal interfaces to the continuum of propagating far-field modes $|m\rangle$ [38], i.e., radiative damping $\Gamma_{\mathrm{r,ij}}$. It is essential that the presence of the slits leads not only to a damping of the individual resonances ($\Gamma_{\mathrm{r},11}$, $\Gamma_{\mathrm{r},22}$) but also causes a radiative coupling ($\Gamma_{\mathrm{r},12}$, $\Gamma_{\mathrm{r},21}$) among the SPP modes via the far-field continuum. Such radiative coupling effects have been the subject of detailed investigations in atom quantum optics [41, 42], yet have so far received little attention in plasmonics. The radiative damping and coupling terms can be cast into a coupled mode matrix with eigenvalues describing the resonances of the coupled system and their radiative decay:

$$\begin{pmatrix} \omega_1 - i\gamma_1 & 0 \\ 0 & \omega_2 - i\gamma_2 \end{pmatrix} + \begin{pmatrix} V_{11} - i\Gamma_{\mathrm{r},11} & V_{12} - i\Gamma_{\mathrm{r},12} \\ V_{21} - i\Gamma_{\mathrm{r},21} & V_{22} - i\Gamma_{\mathrm{r},22} \end{pmatrix} . \qquad (2)$$

The detuning $\Delta(k_x) = \omega_2(k_x) - \omega_1(k_x)$ between the two unperturbed resonances follows from the SPP dispersion relation of the unpatterned film and is continuously varied by angle tuning. For the AM[±1] resonance and small angles, all individual coupling constants $V \simeq V_{\mathrm{ij}}$ are nearly identical, as are the damping constants $\Gamma_{\mathrm{r}} \simeq \Gamma_{\mathrm{r,ij}}$, $\gamma \simeq \gamma_{\mathrm{j}}$. Matrix diagonalization shows that the eigenfrequencies of the coupled modes are then given as $\omega_{+,-} = \omega_1 - i\gamma + \Delta/2 + V - i\Gamma_{\mathrm{r}} \pm A/2$ with $A = \sqrt{\Delta^2 + 4(V - i\Gamma_{\mathrm{r}})^2}$. The resulting coupled (nonnormalized) eigenmodes are $|+, -\rangle = c_{1,\pm}|1\rangle + c_{2,\pm}|2\rangle$, with coefficients $c_{1,\pm} = -(\Delta \mp A)/(2(V - i\Gamma_{\mathrm{r}}))$ and $c_{2,\pm} = 1$. Using this model, one can readily simulate optical transmission spectra using (1), see Fig. 8c.

The coupling between these two resonances results in the opening of the SPP band gaps $2\hbar V$ when the SPP modes are angle-tuned into resonance (Fig. 6). This band gap formation coincides with a pronounced change of the linewidth $\Gamma_{+,-} = \gamma + \Gamma_{\mathrm{r}} \mp \mathrm{Im}(A/2)$ of the newly formed resonances. For the symmetric (bright) $|+\rangle$ mode, the radiative coupling to the far-field continuum $\Gamma_{\mathrm{r},+} = \Gamma_{\mathrm{r}} - \mathrm{Im}(A/2)$ linewidth increases by a factor of two for $\Delta \to 0$ (superradiance). For the antisymmetric (dark) $|-\rangle$ mode, however, the radiative damping $\Gamma_{\mathrm{r},-} = \Gamma_{\mathrm{r}} + \mathrm{Im}(A/2)$ decreases continuously with decreasing detuning, and radiative damping is fully suppressed at $\Delta = 0$. Here, the linewidth of the resonance is no longer limited by radiative damping but by the intrinsic losses γ. In angle-dependent spectra (Fig. 8b), one thus observes a narrowing of the resonance with decreasing θ until $\Gamma_{\mathrm{r},-} < \gamma$, followed by a decrease of the intensity of the dark mode peak, which vanishes at $\Delta = 0$. The results in Fig. 8b,c are satisfactorily modeled by (2) when parameters $\hbar V = 35$ meV and $\hbar\Gamma_{\mathrm{r}} = 13$ meV are assumed. The slightly stronger variation in the experimentally measured linewidth is mainly attributed to an oversimplified modeling of the non-resonant transmission continuum in (1).

The microscopic origin of this pronounced suppression of radiative damping becomes immediately apparent by looking at the spatial near-field mode profiles of the coupled modes (Fig. 9). The mode overlap of the symmetric $|+\rangle$ mode with the nanoslit scattering centers is larger than that of the uncoupled modes $|1, 2\rangle \propto \exp(\pm iGx)$, thus increasing the radiation damping constant $\Gamma_{r,+}$. For the antisymmetric $|-\rangle$ mode, however, the maxima of $I(x) \simeq |\exp(iGx) - \exp(-iGx)|^2$ at $\pm a_0/4$ are now in between the nanoslits. The field intensity at the nanoslits is strongly reduced, and the radiative damping rate $\Gamma_{\mathrm{r},-}$ becomes vanishingly small. This is in analogy to previously observed interference phenomena in the radiative damping of other, e.g., atomic or molecular, multi-level systems [41, 42]. In such systems, however, the finite radiative damping of the uncoupled systems is often larger than their radiative coupling, and the suppression of radiative damping is much less pronounced [41]. In the system considered here, the intrinsic damping is sufficiently weak to reach the strong radiative coupling limit ($\Gamma_{\mathrm{r}} > \gamma$).

A more refined theoretical description of light transmission through nanoslit gratings can be obtained from a full, scattering-matrix-based solution of Maxwell's equations [22]. Such calculations predict that in addition to the SPP-induced resonances, nanoslit arrays should display additional, weakly angle-dependent Fabry–Pérot type resonances [18]. Such resonances occur because sub-wavelength 1D structures support a propagating mode within the nanoslit wave guide channel, in contrast to the evanescent wave guide

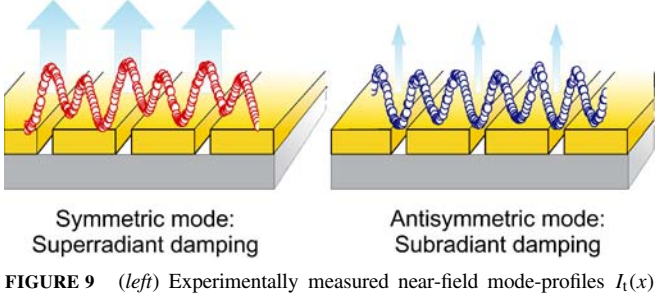

FIGURE 9 (*left*) Experimentally measured near-field mode-profiles $I_{\mathrm{t}}(x)$ of the symmetric mode $|+\rangle$ recorded at an excitation energy of 1.548 eV (superradiant mode). The position of the nanoslits, simultaneously measured by shear-force microscopy, is indicated. (*right*) $I_{\mathrm{t}}(x)$ of the antisymmetric mode $|-\rangle$ at 1.617 eV (subradiant mode). The reduced mode overlap with the nanoslit scattering centers greatly suppresses radiative damping

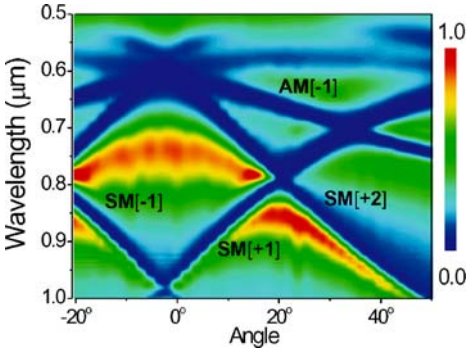

FIGURE 10 Angle-resolved transmission spectrum for a gold nanoslit array with a slit width of 100 nm and grating periods of $a_0 = 537$ nm. For this sample, the thickness of the gold layer is only 75 nm, and an additional, weakly angle-dependent transmission resonance is observed at wavelengths around 750 nm. This new resonance is due to a Fabry–Pérot type interference within the nanoslit waveguide

mode in nanohole arrays. Constructive interference of the partially reflected wave guide mode propagating inside the nanoslit channel results in an enhancement of the direct transmission, the coupling to SPP modes and also of the radiative damping [22]. Such Fabry–Pérot resonances have recently been observed in THz time-domain transmission experiments [43] and in the microwave region [44]. In the visible range, we observed Fabry–Pérot effects on very nanoslit arrays with a film thickness of only 75 nm. As shown in Fig. 10, the transmission spectra display indeed a weakly angle dependent, quite broad transmission resonance around 750 nm. Diffraction theoretical simulations support the assignment of this resonance to the Fabry–Pérot transmission mode. Such calculations also indicate that for the 150 nm thick films studied in Figs. 4–9, this resonance is shifted into the infrared region around 1500 nm and thus has a only weak effect on SPP-based resonances in the visible range and their coupling to far-field radiation. Interesting coupling phenomena are expected when Fabry–Pérot and SPP modes are tuned into resonance, and these phenomena will be the subject of a forthcoming publication.

5 Summary and conclusions

In summary, we have studied the linear optical properties of periodic nanohole and -slit arrays in metal films using both, near-field optical microscopy and ultrafast laser spectroscopy. Ultrafast laser pulses, shorter in duration than the relevant SPP damping times, were transmitted through such arrays, and both, amplitude and phase of the electric field of the transmitted pulses were analyzed. Our experiments give evidence for a pronounced coherent coupling of surface plasmon polaritons in these plasmonic nano-crystals. Near-field optical studies show how the formation of coupled, antisymmetric SPP modes induces an efficient suppression of radiative damping and leads to surprisingly long SPP lifetimes of more than 200 fs. Such a control of radiative damping by tailoring SPP mode profiles is an essential prerequisite for designing and implementing efficient nanoplasmonic devices such as wave guides or resonators, studying the physics of strong SPP localization, or even using SPPs as flying qubits in quantum information processing.

ACKNOWLEDGEMENTS Financial support of the work in Korea by MOST and KOSEF and that in Germany by the Deutsche Forschungsgemeinschaft (SFB296) is gratefully acknowledged.

REFERENCES

1 W.L. Barnes, A. Dereux, T.W. Ebbesen, Nature **424**, 824 (2003)
2 S.A. Maier, P.G. Kik, J.A. Atwater, S. Meltzer, E. Habel, B.E. Koel, A.A.G. Requicha, Nature Mater. **2**, 229 (2003)
3 H.J. Lezec, A. Degion, E. Deveaux, R.A. Linke, L. Martin-Moreno, F.J. Garcia-Vidal, T.W. Ebbesen, Science **297**, 820 (2002)
4 T.W. Ebbesen, H.J. Lezec, H.F. Ghaemi, T. Thio, P.A. Wolff, Nature **391**, 667 (1998)
5 J.B. Pendry, Phys. Rev. Lett. **85**, 3966 (2000)
6 D.S. Kim, S.C. Hohng, V. Malyarchuk, Y.C. Yoon, Y.H. Ahn, K.J. Yee, J.W. Park, J. Kim, Q.H. Park, C. Lienau, Phys. Rev. Lett. **91**, 143 901 (2003)
7 A. Dogariu, T. Thio, L.J. Wang, T.W. Ebbesen, H.J. Lezec, Opt. Lett. **26**, 450 (2001)
8 A. Dogariu, A. Nahata, R. Linke, L. Wang, R. Trebino, Appl. Phys. B **74**, 69 (2002)
9 S.C. Hohng, Y.C. Yoon, D.S. Kim, V. Malyarchuk, R. Müller, C. Lienau, J.W. Park, K.H. Yoo, J. Kim, H.Y. Ryu, Q.H. Park, Appl. Phys. Lett. **81**, 3239 (2002)
10 C. Ropers, D.J. Park, G. Stibenz, G. Steinmeyer, J. Kim, D.S. Kim, C. Lienau, Phys. Rev. Lett. **94**, 113 901 (2005)
11 R.H. Dicke, Phys. Rev. **93**, 99 (1954)
12 C. Iaconis, I.A. Walmsley, Opt. Lett. **23**, 792 (1998)
13 G. Stibenz, G. Steinmeyer, Opt. Express **12**, 6319 (2004)
14 J.-C. Diels, W. Rudolph, *Ultrashort Laser Pulse Phenomena* (Academic Press, San Diego, CA, 1996)
15 F. Reynaud, F. Salin, A. Berthelemy, Opt. Lett. **14**, 275 (1989)
16 L. Lepetit, G. Cheriaux, M. Joffre, J. Opt. Soc. Am. B **12**, 2467 (1995)
17 H.F. Ghaemi, T. Thio, D.E. Grupp, T.W. Ebbesen, H.J. Lezec, Phys. Rev. B **58**, 6779 (1998)
18 A. Porto, F.J. Garcia-Valid, J.B. Pendry, Phys. Rev. Lett. **83**, 2845 (1999)
19 L. Salomon, F. Grillot, A.V. Zayats, F. de Fornel, Phys. Rev. Lett. **86**, 1110 (2001)
20 L. Martin-Moreno, F.J. Garcia-Vidal, H.J. Lezec, K.M. Pellerin, T. Thio, J.B. Pendry, T.W. Ebbesen, Phys. Rev. Lett. **86**, 1114 (2001)
21 Q. Cao, P. Lalanne, Phys. Rev. Lett. **88**, 075 403 (2002)
22 K.G. Lee, Q-Han Park, Phys. Rev. Lett. **95**, 103 902 (2005)
23 H. Räther, *Surface Plasmons* (Springer, Berlin, 1988), Vol. 111
24 T. Thio, H.F. Ghaemi, H.J. Lezec, P.A. Wolff, T.W. Ebbesen, J. Opt. Soc. Am. B **16**, 1743 (1999)
25 A. Taflove, S.C. Hagness, *Computational Electrodynamics. The Finite-Difference Time-Domain Method* (Artech House, Boston, 2000), 2 edn.
26 R. Müller, V. Malyarchuk, C. Lienau, Phys. Rev. B **68**, 205 415 (2003)
27 R. Müller, C. Ropers, C. Lienau, Opt. Express **12**, 5067 (2004)
28 H. Bethe, Phys. Rev. **66**, 163 (1944)
29 C.W. Bouwkamp, Philips Res. Rep. **5**, 321 (1950)
30 A. Bouhelier, M. Beversluis, A. Hartschuh, L. Novotny, Phys. Rev. Lett. **90**, 013 903 (2003)
31 S. Linden, N. Rau, U. Neuberth, A. Naber, M. Wegener, S. Pereira, K. Busch, A. Christ, J. Kuhl, Phys. Rev. B **71**, 245 119 (2005)
32 M.V. Berry, S. Klein, J. Mod. Opt. **43**, 2139 (1996)
33 J.-C. Diels, E.V. Stryland, G. Benedict, Opt. Commun. **25**, 93 (1978)
34 B. Lamprecht, J.R. Krenn, A. Leitner, F.R. Aussenegg, Phys. Rev. Lett. **83**, 4421 (1999)
35 J.H. Chung, A.M. Weiner, IEEE J. Sel. Top. Quantum Electron. **7**, 656 (2001)
36 G. Stibenz, G. Steinmeyer, Opt. Express **13**, 2617 (2005)
37 M. Sarrazin, J.-P. Vigneron, J.-M. Vigoureux, Phys. Rev. B **67**, 085 415 (2003)
38 C. Genet, M.P. van Exter, J.P. Woerdman, Opt. Commun. **225**, 331 (2003)
39 S.G. Tikhodeev, A.L. Yablonskii, E.A. Muljarov, N.A. Gippius, T. Ishihara, Phys. Rev. B **66**, 045 102 (2002)
40 S.G. Johnson, M. Ibanescu, M.A. Skorobogatiy, O. Weisberg, J.D. Joannopoulos, Y. Fink, Phys. Rev. E **65**, 066 611 (2002)
41 R.G. DeVoe, R.G. Brewer, Phys. Rev. Lett. **76**, 2049 (1996)
42 U. Akram, Z. Ficek, S. Swain, Phys. Rev. A **62**, 013 413 (2000)
43 J.W. Lee, M.A. Seo, D.S. Kim, S.C. Jeoung, C. Lienau, J.H. Kang, Q.H. Park, Appl. Phys. Lett. **88**, 071 114 (2006)
44 F. Yang, J.R. Sambles, Phys. Rev. Lett. **83**, 2845 (1999)